scientific reports

Check for updates

OPEN

Denoising of fluorescence lifetime imaging data via principal component analysis

Soheil Soltani[1,5], Jack G. Paulson[1,2,5], Emma J. Fong[1], Shannon M. Mumenthaler[1,3] & Andrea M. Armani[1,2,3,4]✉

Fluorescence Lifetime Imaging Microscopy (FLIM) quantifies autofluorescence lifetime to assess cellular metabolism, therapeutic efficacy, and disease progression. These dynamic and heterogeneous processes complicate signal analysis. Fit-free analysis methods such as phasor analysis are increasingly used due to limitations of fit-based approaches. However, incorporating photon-counting shot noise often leads to moderate-to-high uncertainty in detecting subtle changes. Common noise-reduction strategies can introduce errors and cause data loss. We developed noise-corrected principal component analysis (NC-PCA), which selectively identifies and removes noise to isolate the signal of interest. We validated NC-PCA by analyzing FLIM images of patient-derived colorectal cancer organoids treated with several therapeutics. First, we show NC-PCA decreases uncertainty by up to 5.5-fold compared to conventional analysis and reduces data loss over 50-fold. Then, using a merged dataset, NC-PCA reveals multiple metabolic states. Overall, NC-PCA offers a powerful, generalizable tool to enhance FLIM analysis and improve detection of biologically relevant metabolic changes.

Keywords Principal component analysis, FLIM, Fluorescence lifetime imaging microscopy, Denoising, Organoid imaging, FLIM analysis, Metabolic imaging, Adaptive noise removal, Data retention

Fluorescent Lifetime Imaging Microscopy (FLIM) is a versatile and real-time imaging method used across cell biology, neuroscience, and cancer research[1–3]. This broad impact is due to its ability to reveal information across multiple length scales, allowing dynamic biological processes, cellular structures, and molecular interactions to be measured[4,5]. Over the past several decades, numerous variations of FLIM have been developed by leveraging advances in signal processing, automation, and photodetectors. Unlike conventional imaging which detects the intensity of a fluorescent signal, FLIM analyzes the fluorescent lifetime. In the context of biology, changes in fluorescent lifetimes can be correlated to protein-protein interactions[4,5], fluctuations in pH or temperature[6–8], and molecular dynamics[9,10]. Moreover, FLIM improves the detection of the intrinsic autofluorescence signal that is characteristic of cellular metabolism, enabling fundamental cell biology investigations and advancing therapeutic development[11–13].

Originally, FLIM analysis leveraged exponential fitting methods to extract fluorescent lifetimes, where a linear combination of exponentials was used to fit per-pixel intensity decays[14–16]. While this approach can quantitatively determine the lifetimes and contribution fractions in large datasets, it has high computational costs and high susceptibility to noise resulting in inaccuracies or even convergence errors. These shortcomings led to the development of fit-free analysis methods such as phasor analysis. This strategy translates FLIM data into Fourier space, mapping the per-pixel intensity decay onto orthogonal vectors[16,17]. Any combination of these components corresponds directly to the pixels and represents a unique lifetime combination. This approach can reveal single or multiple dominating lifetimes through clustering in distinct regions on the phasor histogram plot[16,18] with reduced computational load. However, transformations into phasor space inherently integrate the intrinsic counting noise which complicates the identification of distinct clusters and subtle shifts of phasors[19].

Common remedies for noise sensitivity include intensity thresholding (TPA) and a filter-based (FPA) phasor analysis[19,20] (Fig. 1A and B, and S1–S2). While effective for small datasets with low-noise signals, these methods have two main limitations. First, for larger datasets, adaptive thresholding is required to account for varying

[1]Ellison Medical Institute, Los Angeles, CA 90064, USA. [2]Mork Family Department of Chemical Engineering and Materials Science, Viterbi School of Engineering, University of Southern California, Los Angeles, CA 90089, USA. [3]Alfred E. Mann Department of Biomedical Engineering, Viterbi School of Engineering, University of Southern California, Los Angeles, CA 90089, USA. [4]Ming Hsieh Department of Electrical and Computer Engineering – Electrophysics, Viterbi School of Engineering, University of Southern California, Los Angeles, CA 90089, USA. [5]Soheil Soltani and Jack G. Paulson contributed equally to this work. ✉email: aarmani@emila.org

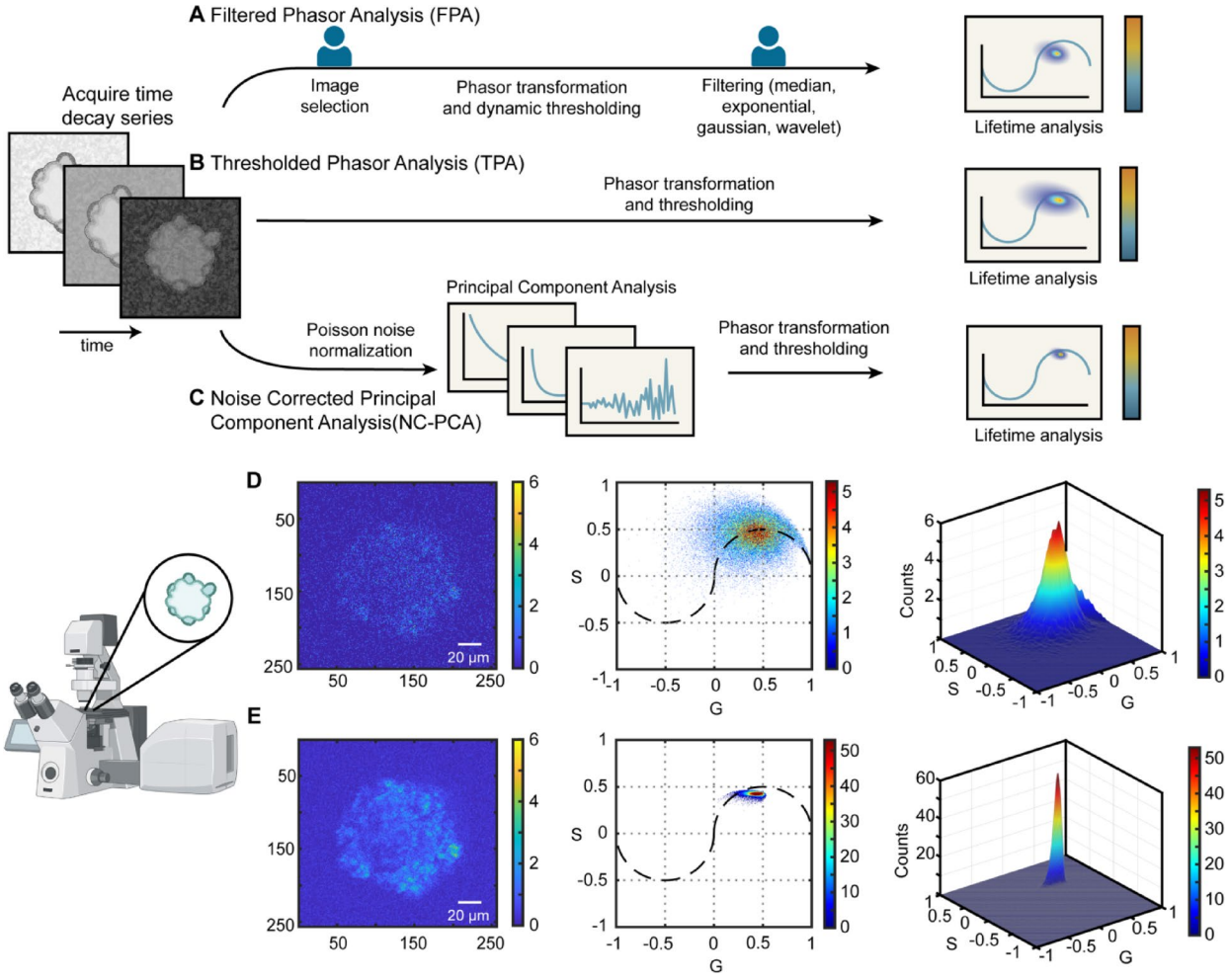

Fig. 1. Phasor analysis workflows for FLIM data. After image acquisition on a FLIM system, the data is analyzed using different approaches. (**A**) Filtered phasor analysis method (FPA) includes image selection based on total counts, dynamic thresholding, and application of a selective smoothing filter. (**B**) Thresholded phasor analysis (TPA) only involves the application of an adaptive threshold. (**C**) Noise-corrected Principal Component Analysis (NC-PCA) begins with a Poisson noise normalization, then application of PCA, and subsequent thresholding and phasor transformation. (**D**) Example of results obtained using the TPA analysis method. First time-bin image of a patient-derived colorectal cancer organoid, 2D phasor histogram, and 3D phasor histogram. Note that a portion of the phasor data lies in the negative domain of the universal circle, which is an unphysical result. (**E**) Example of results obtained using the NC-PCA method. Note the reduction in S and G spread in the NC-PCA phasor plot and the 10x difference in counts between parts (**D**) and (**E**) as a result of the improved phasor clustering. Additionally, all data now lies within the positive region of the universal circle.

noise levels. Second, the common smoothing filters, such as median, exponential, and Gaussian, are susceptible to introducing smoothing errors[21]. Therefore, frequent filter parameter tuning is required. Other noise reduction techniques such as wavelet filtering have shown superior denoising capabilities but involve complexities like wavelet bias selection, parameter tuning, and leakage between bands[22,23]. More recently, machine learning models are being explored as a means of noise reduction[19]. However, these models depend heavily on high-quality, labeled training data for accuracy, which is hard to acquire and is often missing in rapidly emerging fields.

An alternative for analyzing FLIM datasets is a dimensionality reduction method known as Principal Component Analysis (PCA). This technique selectively removes noise while retaining structured data through a transformation into a new orthogonal basis set[24,25], constructed by the eigenvectors and eigenvalues of a mean-centered covariance matrix (Figures S3–S4). These vectors, or principal axes, are sorted in decreasing variance order. Thus, PCA enables precise identification of the important features with the highest variance and facilitates effective removal of noise in complex datasets. Additionally, because it is a data-driven denoising scheme and it does not rely on a priori knowledge of the system[26], it removes potential bias. As a result, PCA has been applied in a diverse array of fields, including data and image compression, omics research, and financial analysis[27–29].

To date, the application of PCA to the analysis of microscopy data in the biomedical domain has relied on fluorescently-labeled samples[27]. These data sets have high photon counts or high signal to noise ratios. However, when capturing dynamic information about a biological system, the photon count is typically low due to either the number of frames used for a given timepoint or the type of signal being analyzed. For example, the autofluorescence signal is much weaker than a signal generated by a synthetic fluorophore. One approach to increase the signal is to increase the laser power; however, this strategy results in sample damage through phototoxicity. Therefore, developing a PCA approach for analyzing low photon count data will advance a range of imaging studies. In the present work, we develop a noise-corrected-PCA (NC-PCA) method for denoising low photon count FLIM data and validate the approach using both simulated and experimental images (Fig. 1C). Our NC-PCA analysis technique simultaneously denoises time-domain FLIM signals and enhances phasor domain accuracy (Fig. 1D and E) by reducing Shot noise and preserving the correlated linearity of corresponding pixels[27,30–32]. Moreover, as shown in Fig. 1C, NC-PCA can be directly integrated into a standard FLIM analysis workflow. To confirm the method, we created and analyzed synthetic FLIM data as well as a standard fluorescent dye with known ground truth values. Next, we used the NC-PCA method to analyze more than 800 patient-derived colorectal cancer organoids and confirmed the improvement in performance as compared to the TPA approach. We showed that data retention is improved by ~ 50-fold and the uncertainty is reduced by ~ 5-fold. Finally, we analyzed the metabolic activity of patient-derived colorectal cancer organoids in response to standard therapeutics using all three approaches. In comparison to TPA and FPA, NC-PCA demonstrated a reduction in error as high as ~ 58% and ~ 45%, respectively. Finally, using an overlaid dataset consisting of untreated and treated organoids, we demonstrated that NC-PCA can resolve multiple emission lifetimes which are indicative of distinctly different metabolic states.

Results

Validation of NC-PCA using synthetic data

To demonstrate the effectiveness of NC-PCA for FLIM noise reduction, we generated a synthetic time-series dataset based on a 540 × 720 pixel image of a cell. The image included distinct geometric features representing cellular structures such as the nucleus, mitochondria, vacuoles, ribosomes, and cell wall. Each nonzero pixel was assigned a fluorescence lifetime that governed its exponential decay (Table S1). Using these lifetimes, we simulated a 256-frame time-series with pixel intensities decaying over time to model fluorescence lifetime behavior. This dataset served as a ground truth reference for evaluating NC-PCA's reconstruction and denoising accuracy. Figure 2 A shows the first time bin of the ground truth. To create a synthetic experimental image from this ground truth, we evaluated both the signal and the noise.

The noise distribution present in FLIM data is primarily Poisson noise, commonly referred to as Shot noise, where noise arises from counting errors with a standard deviation proportional to the square root of photon counts[32]. To simulate this, we applied a randomized Poisson distribution to each pixel, using the corresponding time-bin photon count as the mean value. For background pixels with no assigned lifetime, a mean of 0.8 was used to ensure nonzero noise, based on experimental results (see SI).

Since the signal-to-noise ratio (SNR) of Shot noise scales with square root of photon counts, we varied the noise characteristics by adjusting the total photon counts for every decay signal per pixel. The range of total counts per image was chosen to reflect observed values in experimental datasets with representative photon counts ranging from 80 to 1000 photons. This approach ensured that our synthetic data accurately modeled the variations in photon signal strength as well as noise encountered in experimental FLIM data. Additional details are provided in the SI.

As a representative example, Fig. 2B C show the first time bin of the synthetic data with 200 photon counts and the corresponding NC-PCA reconstruction. Signal-to-noise ratio (SNR) and mean square error (MSE) are complementary metrics for evaluating reconstruction quality. Higher SNR reflects more robust reconstruction; lower MSE indicates greater similarity. Both metrics were computed for the raw and the NC-PCA reconstructed images by analyzing pixel intensity values across all time bins.

Figure 2D highlights the decay of the highest intensity pixel, revealing substantial signal quality improvements after NC-PCA reconstruction. The SNR increased nearly threefold, from 5.99 dB in the synthetic image to 17.5 dB post-reconstruction. Similarly, MSE dropped over an order of magnitude, from 1.34 to 0.05. These results underscore NC-PCA's ability to enhance signal fidelity, especially in low-photon-count pixels. This ability will directly advance applications where data acquisition speed is a priority, such as monitoring dynamic biological systems.

Similar analysis can be performed for the entire dataset which encompasses 388,800 pixels over 256 time bins. The results from this spatial analysis are detailed in Fig. 2E and H. Figure 2E and F display the MSE before and after NC-PCA reconstruction while Fig. 2G and H present the corresponding SNR. To allow direct comparison between the figures, the scale bars are unified. Quantitatively, the median MSE decreases from 0.875 in Fig. 2E to 0.0101 after NC-PCA reconstruction (Fig. 2F). In parallel, the median SNR in the synthetic dataset Fig. 2G is 1.87 dB, which improves to 21.2 dB post NC-PCA reconstruction (Fig. 2H). Taken together, NC-PCA results in nearly a ~ 20 dB improvement in SNR and ~ 90x improvement in MSE.

To further evaluate NC-PCA in FLIM analysis, we assessed the improvements in SNR and MSE as the photon counts increased from 80 photon counts (low SNR) to 1800 photon counts (high SNR). Increasing the photon counts in the model serves as a proxy for increasing the frame number in an experiment. The synthetic images over this entire photon count range, their NC-PCA reconstructed counterparts, and the corresponding MSE and SNR maps are provided in Figure S5 and S6. The distributions of SNR and MSE at each photon count level are shown in the violin plots in Figure S7, and a subset of the data is presented in Fig. 2I J. As can be observed, the SNR and MSE improvement enabled by NC-PCA is maintained over the entire range studied.

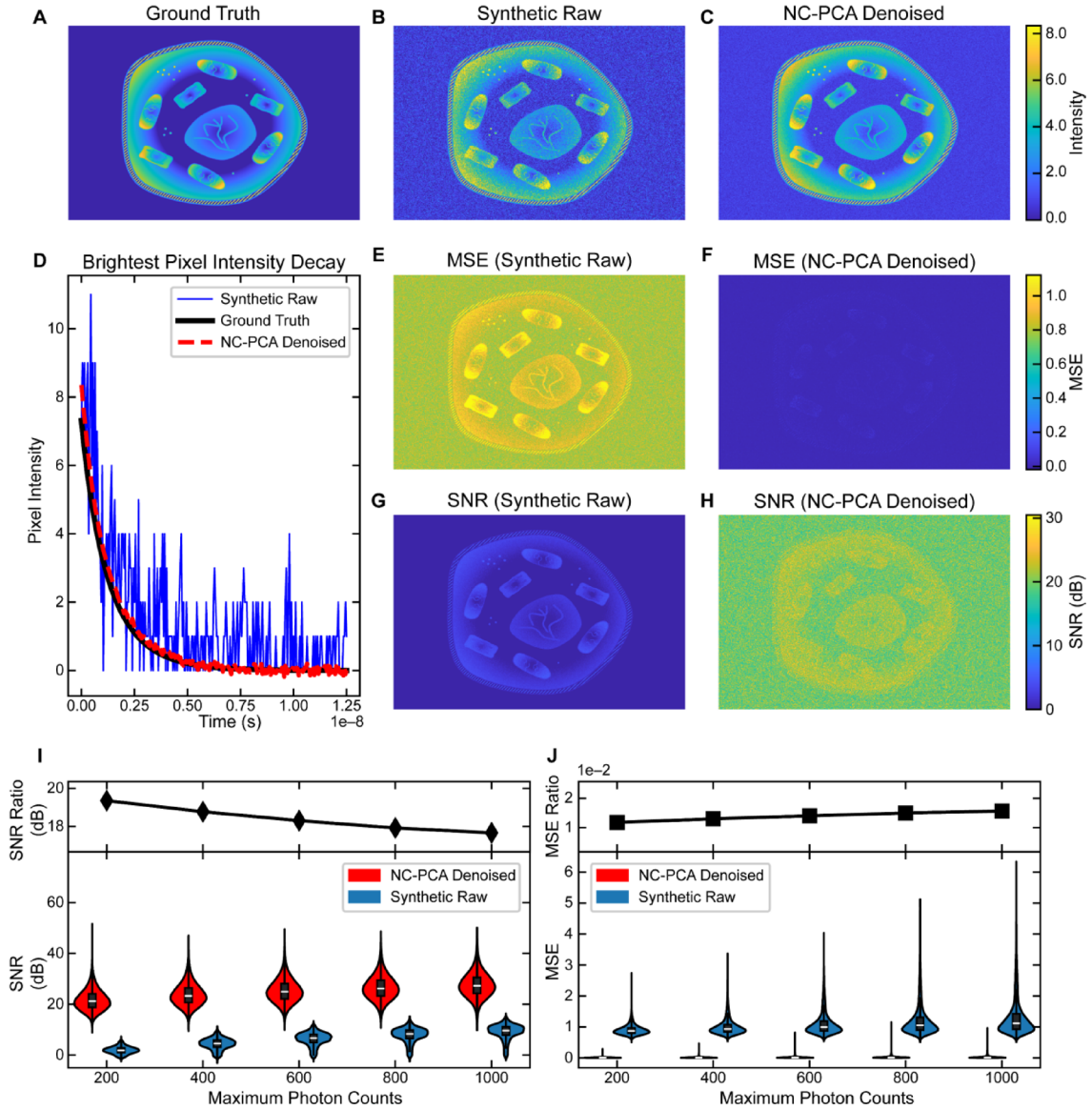

Fig. 2. Ground truth comparison of NC-PCA on synthetic FLIM data. The first time bin of the synthetically created data that serves as the (**A**) ground truth and (**B**) that is modified with Poisson noise to serve as the synthetic raw data. A range of photon count levels were investigated, and this representative data is limited to 200 photon counts, representing extremely noisy data. (**C**) The image shown in part (**B**) is reconstructed using NC-PCA. (**D**) The intensity of the brightest pixel in the ground truth image (solid black), synthetic raw data (solid blue), the NC-PCA (red dashed). (**E**, **F**) MSE and (**G**, **H**) SNR are calculated for each pixel across the entire synthetic raw image or NC-PCA reconstructed image. (**I**, **J**) To explore the role of noise in reconstruction ability, the photon counts were varied from 80 photon counts (low SNR) to 1800 photon counts (high SNR). All results are included in the SI, and a subset of the results are presented. The violin plots for (**I**) SNR and (**J**) MSE images from synthetic raw and NC-PCA reconstruction images highlighting the improvement offered by NC-PCA, in terms of data spread and relative SNR and MSE values. NC-PCA improvement was quantified via SNR and MSE Ratios between synthetic raw and NC-PCA reconstruction.

To quantify the performance of NC-PCA, we define two metrics: SNR ratio and MSE ratio. The former, expressed in decibels, is the difference between the median SNR of the NC-PCA reconstruction and the noise-embedded synthetic data. The latter is the median MSE of the NC-PCA reconstruction divided by the noise-embedded synthetic data. These values are calculated for the entire data set. As shown in Fig. 2I and J, and S5-S7, both metrics indicate clear improvement across all photon counts. As photon counts increase, the noise-embedded synthetic SNR improves, bringing decay signals closer to the ground truth. Thus, while NC-PCA consistently enhances SNR and MSE, the degree of improvement lessens at higher photon counts.

To evaluate the computational savings, we compared end-to-end computation time on a simulated time series similar to the one shown in Fig. 2. This data series is comprised of simulated FLIM data (256 time bins, 256×256 pixels) with mono-exponential decays including Poissonian noise. The known lifetime is 2.5 ± 0.1 ns,

similar to Coumarin-6 dye. The total data set included over 65,000 individual pixel decays. To enable a direct comparison among methods, all computations were performed on the same computer (same CPU). The data was analyzed using four different methods: NC-PCA, Median (3 × 3 window size, phasor domain), exponential fitting (time domain using Maximum Likelihood Estimation), and Wavelet (phasor domain using Complex Wavelet Filter). While all methods were able to converge on the correct lifetime value, NC-PCA reached the correct value in the shortest amount of time. For example, NC-PCA is 1.6x faster than the wavelet approach. Additional details, including convergence graphs, are in the SI (Table S2, Figure S8).

Validation of NC-PCA approach using experimental FLIM data

When imaging dynamic biological systems using FLIM, the number of acquired frames is often lowered to maintain acceptable image acquisition rates. For example, the number of acquired frames in our system is normally within the range of 10–30 frames which allows the minimum total counts per pixel to be greater than 100. By increasing the number of acquired frames to ~100–200 frames, the total photon count increases to 7,000–10,000, and the accuracy of the data analysis improves. However, this increase in frame number dramatically increases the image acquisition time up to 10-fold, which negatively impacts the ability to capture dynamic information.

To confirm that NC-PCA can reliably reconstruct a low frame or low photon count dataset, a solution containing a single fluorophore, Coumarin-6, was imaged with two frame acquisition values: 30 and 100. All other conditions, including sample preparation and microscope settings, were identical between the measurements. The decrease in noise during the 100-frame measurement allowed this data to serve as ground truth. To obtain lifetime values, a single component exponential fit was applied to every pixel in each image. In addition, NC-PCA was performed on the 30-frame acquisition data. Prior work has demonstrated that Coumarin-6 exhibits a single fluorescence decay pathway with lifetime values in the range of 2.43–2.60 ns[33,34]. Because only one lifetime is present, the phasor distribution should be located on the unit circle, and this fluorophore provides an ideal experimental testbed to evaluate the NC-PCA method.

We have calculated the phasor histograms for the 100-frame ground truth, raw 30-frame, and PCA reconstructed Coumarin-6 images. The results are shown in Fig. 3A and C. To quantitatively assess the data spread, the FWHM along the G axes is calculated for each dataset. The FWHM in the data significantly increases from 0.061 to 0.2217 when the frame decreases from 100-frame to 30-frame (Fig. 3A and C). However, when NC-PCA is applied to the 30-frame data, the FWHM is reduced to 0.086, which is comparable to the 100-frame

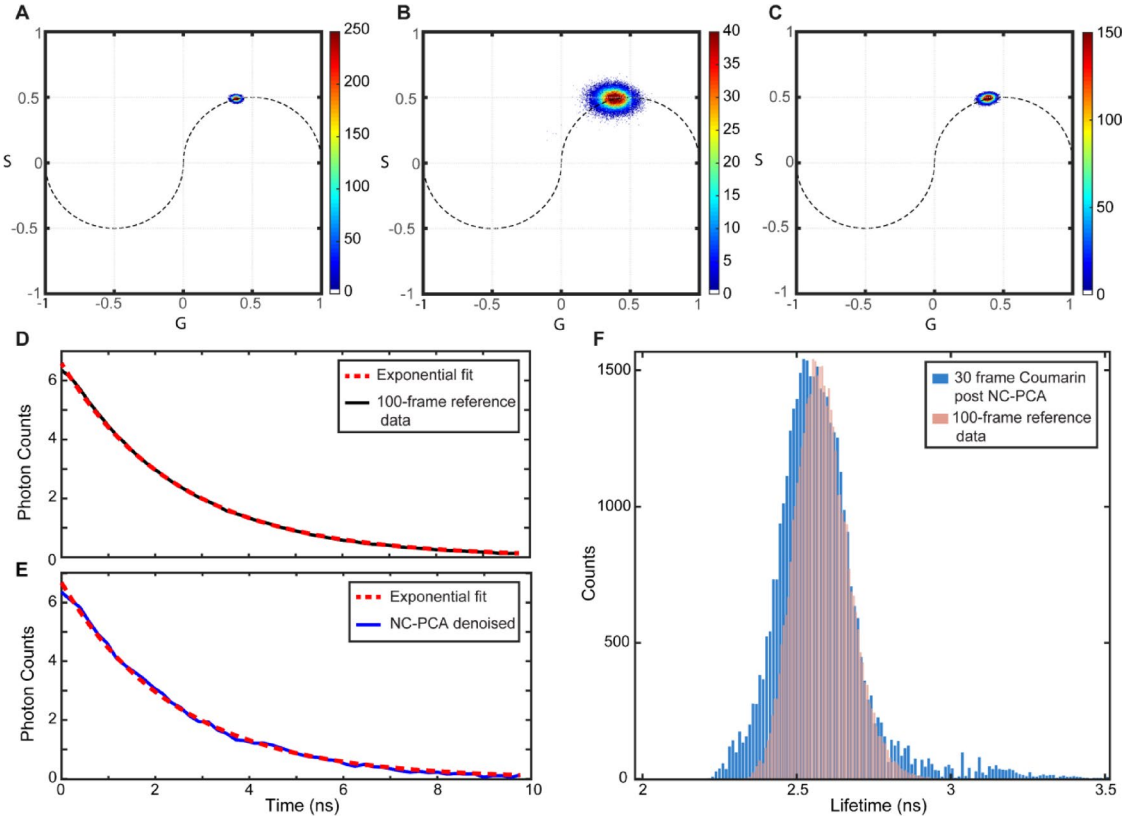

Fig. 3. Comparison of lifetime distribution between the 100-frame ground truth FLIM signal and 30-frame raw data post NC-PCA reconstruction for Coumarin-6. Phasor histograms for (**A**) 100-frame ground truth (**B**) 30- frame raw data (**C**) 30-frame raw data post NC-PCA reconstruction. Representative temporal decay FLIM signal overlaid on single exponential fit for (**D**) 100 frame ground truth (**E**) 30 frame raw data post PCA reconstruction. (**F**) comparison of histograms for extracted lifetimes from 100-frame ground truth and post NC-PCA denoising for 30-frame Coumarin-6 FLIM images.

ground truth. Thus, NC-PCA effectively reduces the noise content in the raw low photon data, reducing the uncertainty in the phasor histogram. These results demonstrate that NC-PCA allows 30-frame data to achieve a similar fidelity to the 100-frame ground truth, enabling faster acquisition rates with minimal degradation in accuracy.

In addition, we fit temporal intensity decays on a per pixel basis and for the entire distribution of lifetimes. Figure 3D presents a representative decay for the 100-frame ground truth data that is fit to a single exponential decay. Attempts to fit the raw 30-frame data were unsuccessful because they either did not converge or resulted in large error due to insufficient signal-to-noise ratios. However, after applying NC-PCA to the 30-frame data, the previously obscured signal became clearly identifiable, and the data could be reliably fit (Fig. 3E). Thus, the subsequent discussion focuses on a comparison between the 100-frame ground truth data and the NC-PCA analyzed 30-frame data.

Figure 3F shows the lifetime distribution from the ground truth image and from the NC-PCA reconstructed 30-frame FLIM image. The histogram of ground truth values has a mean of 2.58 ns and a Full Width Half Maximum (FWHM) of 0.2 ns. In comparison, the histogram of the NC-PCA constructed 30-frame data yields a mean lifetime of 2.56 ns and a FWHM of 0.23 ns. Both values are in agreement with prior results and are self-consistent[33,34].

Validation of NC-PCA approach using patient-derived colorectal cancer organoids

FLIM imaging is routinely used to evaluate a biological system's response to a perturbation by performing a phasor transformation of FLIM data and analyzing two variables, G and S. Together, these parameters represent the position and direction of shifts on the phasor histogram. The shifts reveal information regarding the fluorescent lifetime of different components in a sample which can be correlated to changes in metabolic activity[11,13,35,36]. Notably, only data that falls within the positive domain of the universal unit circle is physically realizable. To isolate this signal, researchers frequently remove results with negative values by applying aggressive filters to their data and only present the positive-valued FLIM results. In this work, to highlight the effect of noise in spreading the distribution of the data the entire universal unit circle is plotted, and all data is presented.

When a single lifetime is present, G and S fall directly on the universal unit circle, as seen in the Coumarin-6 data (Fig. 3). Shorter lifetimes lie near the edge (G = 1, S = 0) while longer lifetimes are closer to the origin. Points inside the unit circle represent weighted sums of lifetimes on the circle. Therefore, the phasor histogram position reflects the sample's exact lifetime composition. However, decay signal noise in each pixel broadens the histogram and limits measurement accuracy[15,37].

The ability of NC-PCA to overcome this limitation is demonstrated by temporally de-noising FLIM signals from patient-derived colorectal cancer organoids. Similar to the previous measurement, we used 100-frame data as the ground truth and 10-frame imaging with and without NC-PCA for the experimental measurement. All other conditions, including sample preparation and microscope settings, were identical between the measurements (SI, Table S3–S4). The first time-bin images for all three measurements are shown in Fig. 4A and C, and the associated phasor plots are in Fig. 4D and F.

Qualitatively, the G and S data, cluster around similar values across all three phasor plots; however, the 10-frame dataset shows a significantly broader distribution. To quantify the similarities and differences, we calculated the median count coordinates and FWHM along the G and S axes (Fig. 4D and F). The NC-PCA denoised 10-frame data differs from the 100-frame ground truth by less than 0.3% in G and 0.25% in S. Additionally, the FWHM for the 10-frame data is 0.276 and reduces nearly 5x to 0.052 after NC-PCA denoising. This value is comparable to the FWHM of the ground truth which is ~ 0.03. Therefore, NC-PCA reduces the data uncertainty while maintaining the median values.

It is important to highlight that NC-PCA effectively reduces variance while preserving the underlying decay structure, thereby correcting the subtle skew introduced by very low–photon-count pixels in the phasor histogram. As a result, the phasor distribution shifts closer to the ground truth. This seemingly modest yet critical improvement was consistently observed across all low-photon-count FLIM images when a high-photon-count ground truth was available. Importantly, despite this change, the median phasor values remain very small and negligible with no effect in metabolic state estimation (maximum ~ 0.02 in G or S direction).

The quality of the reconstruction was further quantified by calculating the SNR and MSE at the single pixel level (Fig. 4G) and across the entire dataset (Fig. 4H and K) using the 100-frame dataset as the ground truth. For the given pixel, the SNR increased by 9.7dB, and the MSE decreases by ~ 9.4 fold when the NC-PCA method is applied to the 10-frame dataset. When the entire dataset is evaluated, similar trends in SNR (Fig. 4H and I) and MSE (Fig. 4J and K) are observed. We find an average improvement in the SNR by ~ 10 dB and a decrease in MSE by ~ 10 fold.

Additionally, NC-PCA reconstruction adaptively denoises the low frame FLIM signal, resulting in an improvement in the time domain data and consequently, in the fit-free phasor domains. This improvement significantly enhances the phasor domain detection accuracy with no information lost during the process. Notably, the phasor domain detection resolution improved from 0.276 to 0.052 even as the frame number decreased from 100- to 10-frames.

Assessment of data loss

One application of FLIM imaging is evaluating metabolic changes in biological systems. In combination with 3D cultures, this method is frequently used as part of a therapeutic development pipeline. For the specific case of imaging cellular metabolism, the change in autofluorescent emission of NADH as it shifts between free and protein-bound states is often leveraged[12,36,38]. Because these two states have distinctly different autofluorescent lifetimes, it is possible to detect metabolic changes by monitoring the phasor histogram. Typically, the results are reported in terms of the fraction bound (fB) NADH, which is directly proportional to G and S (Figure S9–S10).

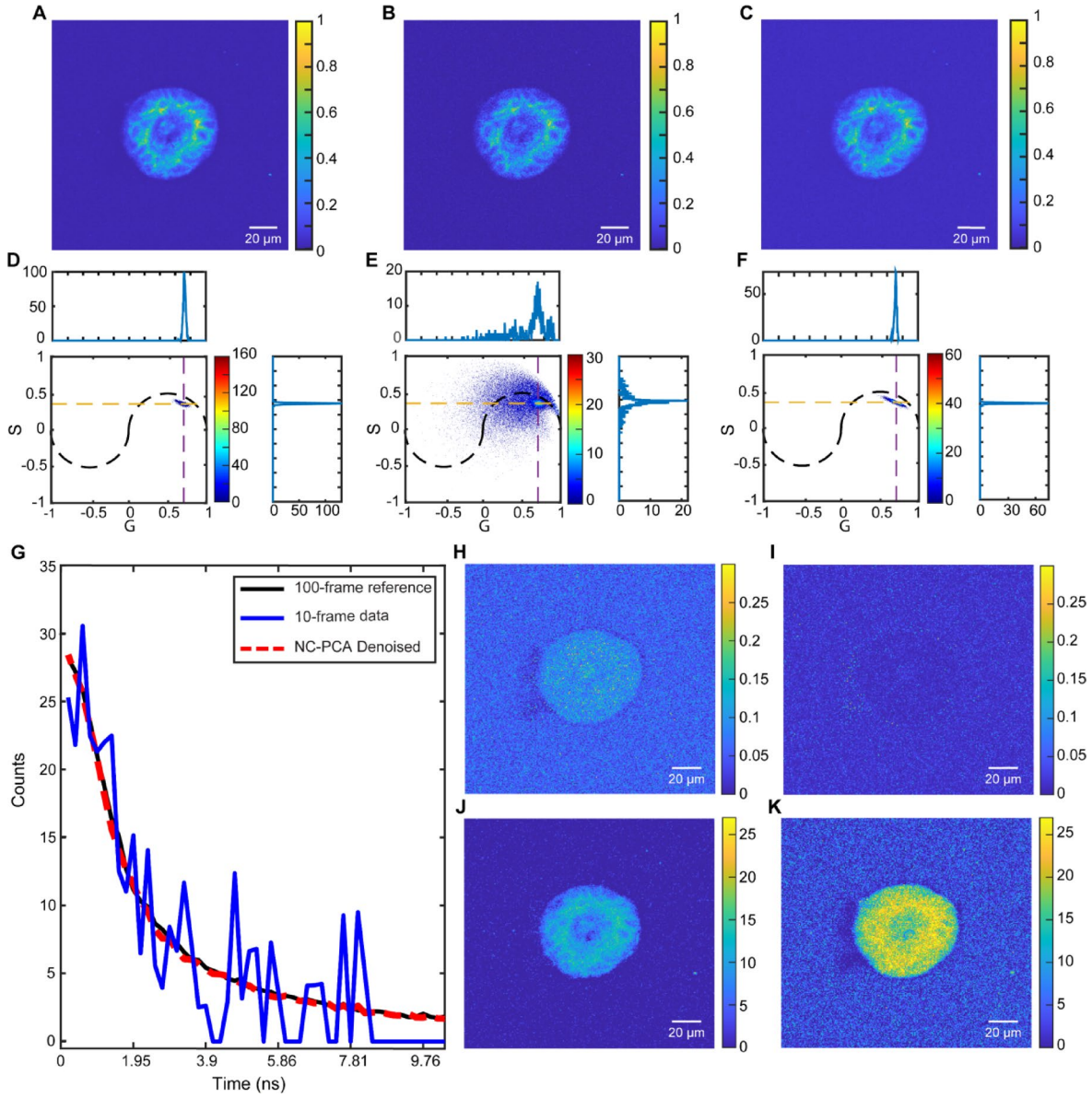

Fig. 4. Application of NC-PCA on a patient-derived colorectal cancer organoid. FLIM images of (**A**) 100-frame FLIM data used as low-noise reference data, (**B**) 10-frame FLIM data, and (**C**) NC-PCA denoised 10-frame FLIM data. (**D–F**) Phasor plot of (**D**) reference data, (**E**) 10-frame FLIM data, and (**F**) NC-PCA denoised 10-frame FLIM data. The median count coordinates and the FWHM along the G and S axes are calculated along the dashed lines (**G**) The intensity of the brightest pixel in the reference image (solid black), 10-frame image (solid blue), and NC-reconstruction (red dashed) tracked over time. (**H**, **I**) MSE and (**J**, **K**) SNR are calculated for each pixel across the entire (**H**, **J**) 10-frame image and (**I**, **K**) NC-PCA reconstructed image using the 100-frame data set as the reference.

Like many biological imaging measurements, these metabolic FLIM datasets can suffer from significant variable noise which is integrated directly into G and S. In efforts to simplify the interpretation and increase statistical confidence, the phasor distribution is often collapsed into a single pair of S and G values post-filtering. This technique requires that the entire phasor distribution of each image is averaged, and the histogram state of the image is then approximated by a single pair of values. This approach simplifies the phasor plot and may lead to a loss of information. NC-PCA provides a path to reduce the impact of detector noise while maintaining the complexity of the lifetime data, improving data analysis rigor.

To evaluate the impact of post-filter averaging and demonstrate the capability of NC-PCA to obviate the need for single-point approximation, we calculated the phasor histograms of a representative image using either the FPA or NC-PCA phasor histogram methods. Figure 5A and C presents the phasor histogram, G, and fB images, respectively, of the FLIM data processed using the FPA process outlined in Fig. 1A. Figure 5D and F shows the same image processed using the NC-PCA method (see SI for details).

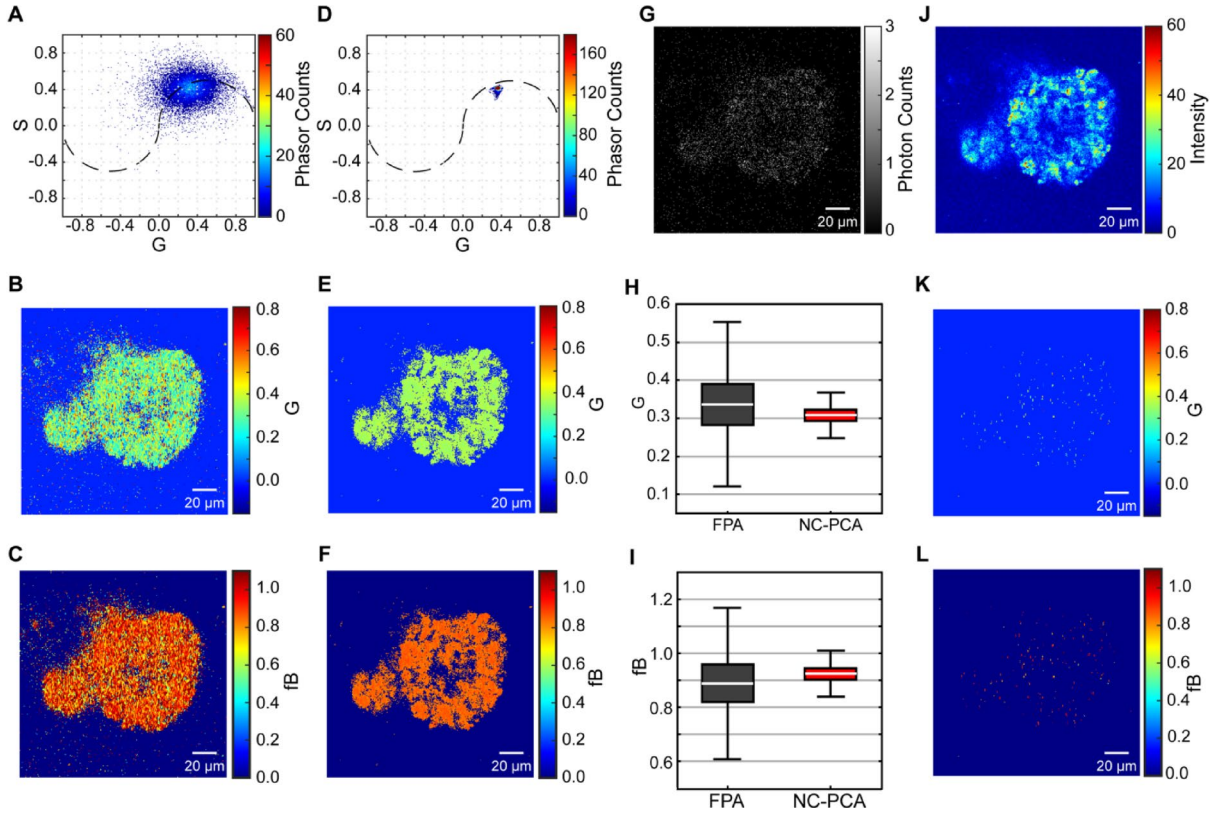

Fig. 5. Comparison of phasor distributions of a organoid using filtered phasor analysis and NC-PCA analysis. Phasor histogram, G value, and fraction bound images of a organoid analyzed using (**A-C**) filtered phasor analysis and (**D–F**) NC-PCA analysis. (**G**) Grey scale image of the first plane photon count. (**H**, **I**) comparison of boxplots for G value and fraction bound distributions using FPA and NC-PCA phasor analysis methods. (**J**) Total photon count per pixel of the same FLIM image used in (**A**). Pixel maps of G values (**K**) and fraction bound (**L**) images highlighting the pixels that preserve their original values if the entire phasor histogram is approximated by average G and S values (data preservation map).

While applying a median filter helps localize the phasor histogram and smooths the G and fB images, the resulting distributions still display significant spread (Fig. 5A and C). This ambiguity highlights the limitation of the median filter in denoising and necessitates aggressive thresholding, filtering, and subsequent phasor averaging. In contrast, the NC-PCA method effectively denoises the phasor histogram, as well as the G and fB images, reducing the uncertainty and spread of phasor distribution (Fig. 5D and F). Therefore, NC-PCA precludes the need for post-filter averaging.

The effective denoising capabilities of NC-PCA compared to FPA is further illustrated when the images obtained using both methods are compared. The G and fB images obtained from filtered phasor analysis (Fig. 5B and C) closely resemble the first time-bin image which is a noisy representative of the FLIM image (Fig. 5G). In contrast, the NC-PCA derived G and fB images (Fig. 5E and F) align more closely with the total photon count map (Fig. 5J). Because the total count map represents and aggressively filtered view of the data, this similarity illustrates that NC-PCA achieves a higher level of denoising than FPA.

The reduction in the phasor distribution using NC-PCA is also quantitatively illustrated in Fig. 5H and I where the boxplots of G and fB are shown. There is a ~ 5-fold reduction in the standard deviation of the G component and fB distributions using NC-PCA compared to the FPA method. This highlights the limitation of FPA method in denoising and necessitates frequent manual adjustment of filter parameters and continuous evaluation for data loss, underscoring its limited utility compared to NC-PCA.

To show the degree of data loss incurred through the FPA process, we have calculated the map of the G and fB values that maintain their original values in case the phasor histogram is averaged and approximated by a single pair of G and S. As clearly highlighted in Fig. 5K and L, less than 2% of data points in G and fB maps are preserved throughout averaging post the FPA process, emphasizing the fact that averaging the FLIM histogram can result in over smoothing and significant data loss. In contrast, NC-PCA effectively denoises the FLIM data such that the uncertainty in the phasor histogram reduces to a degree that averaging is no longer required and averaging errors are obviated. As a result, the data is preserved when NC-PCA is used.

A key feature of NC-PCA, evident in Figs. 1D–E and 3C, and 4D, is its effect on the phasor distribution shape. NC-PCA operates per pixel in the time domain as a linear projection, not as a spatial or phasor-space smoothing filter. It neither averages neighboring pixels nor applies kernels on the phasor histogram. Because NC-PCA mapping is linear along the time axis, any linear mixture of decays, if present, remains a linear mixture after

Treatment	Treatment concentrations
Staurosporine (STS)	0.01 µM, 0.1 µM, 1 µM, and 10 µM
5-fluorouracil (5-FU)	0.1 µM, 1 µM, and 10 µM
7-ethyl-10-hydroxycamtothecin (SN-38)	0.01 µM, 0.1 µM, 1 µM, and 10 µM
Cetuximab (CTX)	0.01 µg/mL, 0.1 µg/mL, 1 µg/mL, and 10 µg/mL
3-bromopyruvate (3-BP)	25 µM, 50 µM, 80 µM, and 100 µM
7-ethyl-10-hydroxycamtothecin (SN-38)	0.01 µM, 0.1 µM, 1 µM, 10 µM
Untreated	

Table 1. Co-varied experimental conditions.

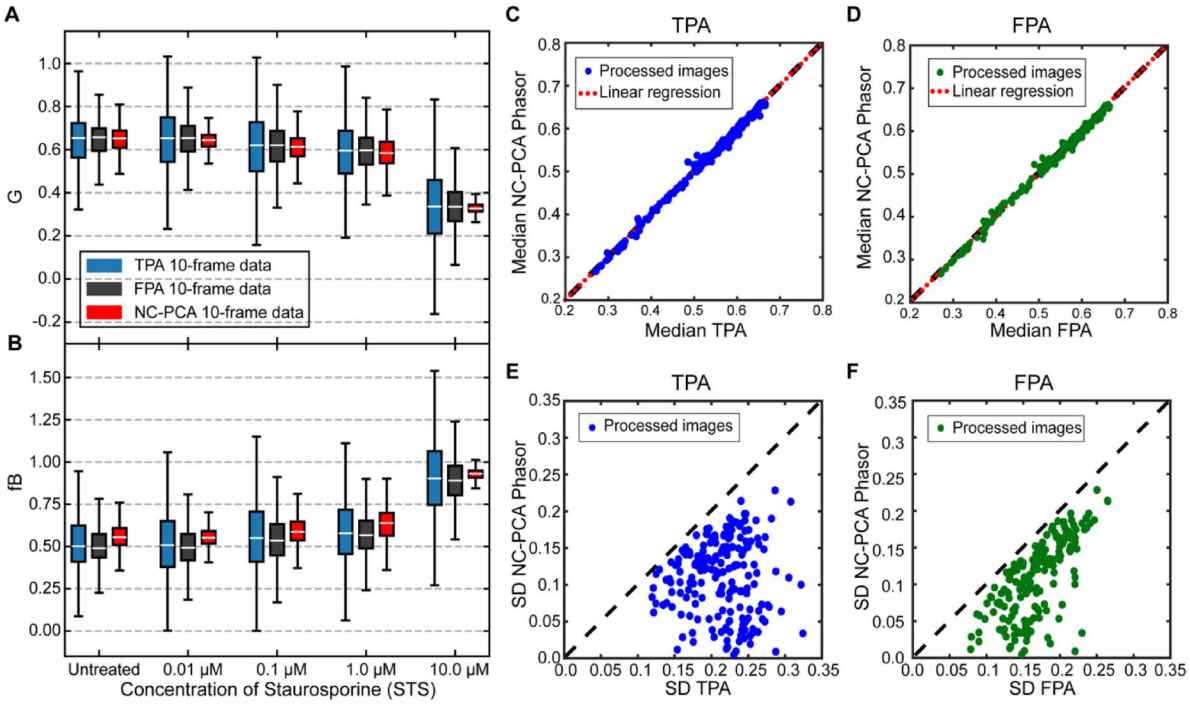

Fig. 6. Statistical analysis of phasor distributions with and without NC-PCA. (**A**) Boxplot of G component of phasors using TPA (blue), FPA (grey), and NC-PCA denoised data (red) for untreated, 0.01, 0.1, 1, and 10.0 µM of STS. (**B**) Box plots of fraction bound values using TPA (blue), FPA (grey) and phasor analysis of the same data after NC-PCA denoising (red), (**C**, **D**) Comparison of median values for G between NC-PCA vs. FPA and TPA respectively. The y = x (black dash) and linear regression fit (red dotted line) are shown for comparison. (**E**, **F**) Comparison of standard deviation for G values between NC-PCA vs. FPA and TPA respectively. As a reference, the line y = x is shown in black dash.

reconstruction. By reducing per-pixel variance dominated by Poisson (shot) noise in FLIM, NC-PCA improves phasor distribution accuracy, suppressing noise-induced broadening and revealing the true multi-component structure aligned with lifetime compositional variations.

Revealing metabolic dynamics and improved resolution of drug effects

While detecting extreme metabolic responses confirms that a response occurs, fully understanding a physiological system requires mapping the entire dose-response curve. To demonstrate NC-PCA's capability for such analysis, we used an existing dataset of patient-derived colorectal cancer organoids treated with various therapeutics along with a control solution (untreated)[36]. A summary of all conditions is shown in Table 1 and Table S4. The total dataset consisted of 207 total images with over 6 million data points. The results for one therapeutic are shown in Fig. 6, and additional analysis for all therapeutics and concentrations studied are in the SI (Figure S11–S14).

As discussed previously, TPA or FPA methods can result in spread or even skewed phasors that have data that is outside physically realizable values due to the incorporation of noise. As shown in Fig. 6A and B, all NC-PCA-reconstruction values fall within the biologically realizable range whereas some values determined using TPA or FPA are non-physical.

A key aspect of any denoising or filtering method is that it should preserve the information and the structure of the data. Based on the prior measurements, we expect that NC-PCA should have a negligible effect on the

median values for single cluster phasor distributions and simultaneously reduce the noise-associated spread. In Fig. 6A and B, it appears that NC-PCA does not significantly change the median values in G and fB. To quantitatively determine if the data median is preserved, we create a single pooled dataset using all the STS-treated organoids in all the conditions (size $n = 207$ images), analyze it using TPA, FPA and NC-PCA phasor analysis methods, and evaluate the median values of G. The calculated slopes are 1.0097 and 0.998 for Fig. 6C and D, respectively. A slope of 1 means that the x and y axis values are identical. Thus, these slope values confirm that the data is preserved across all experimental conditions when NC-PCA is used.

The overarching goal of the NC-PCA method is to reduce the error. As can be observed in Fig. 6A and B, the NC-PCA-driven workflow results in a reduction in both the upper and lower quartiles as well as in whisker length across all STS concentrations studied. To evaluate this metric more broadly, the standard deviation (SD) of G of the pooled dataset was calculated. There is a notable decrease in SD for all datasets when NC-PCA is used (Fig. 6E and F). Taken together, the results in Fig. 6C and F show that NC-PCA effectively preserves key information from the dataset while decreasing uncertainty.

Lastly, by comparing the SD values in Fig. 6E and F, an interesting feature of the NC-PCA method becomes more evident. The SD values calculated for the FPA method are smaller compared to TPA method; however, NC-PCA produces the smallest standard deviation among the methods. This signifies the fact that while filters can remove noise to certain extent, their ability is limited and is not as effective as the NC-PCA method. This fact proves that NC-PCA can efficiently denoise the data with no need for extreme thresholding nor truncation of lower ranked principal components.

In the context of FLIM analysis, the minimum resolvable signal change on the phasor histogram is the FWHM or signal linewidth of the phasor accumulation point. Broad phasor distributions limit the ability to detect subtle metabolic responses within the same image. To demonstrate the ability of NC-PCA to overcome this challenge, a subset of the data in Fig. 6 was used. Specifically, 10 datasets of untreated and 72 h, 10μM STS-treated organoids are calculated and then merged, creating an overlaid dataset that contains two known metabolic states. Figure 7A and D show a representative first time-bin image and phasor histogram of a patient derived organoid processed using TPA and NC-PCA methods. Note that FPA is not a reversible process, and reconstruction of images is not possible. Therefore, reconstructions are limited to TPA and NC-PCA. Phasor plots of the whole dataset were analyzed (Fig. 7E, F and H, and 7I) and subsequently overlaid (Fig. 7G and J). In parallel, the histogram of the data along the G axis was calculated and is plotted as part of Fig. 7E and J.

As evident in Fig. 7E and F, the two phasor distributions generated using FPA have significant overlap. Based on the FWHM of the associated histograms, the minimum detectable signal change on the histogram is limited to 0.5446. In Fig. 7G, the separation distance between these histograms, defined as the difference in G-coordinates of their maximum counts, is ~ 0.31. This separation is nearly half the FWHM value. This analysis highlights why multiple metabolic states, or the metabolic heterogeneity within a single frame, is not distinguishable when FPA is used. This constraint arises from the limitation of the FPA process in denoising.

In contrast, NC-PCA effectively denoises the FLIM data and reduces the phasor histogram FWHM (Fig. 7H and J). As a result, while the separation between the two states is unchanged, the signal linewidth narrows to 0.105. This results in a ~ 5.5 times improvement in linewidth as compared to FPA method, and it is ~ 3 times smaller than the separation distance, making the two states fully resolvable. Importantly, the differences in the mean values of G as determined by both methods are not statistically significant, indicating that the NC-PCA method is not altering the data. Thus, NC-PCA can reveal multiple metabolic processes happening within a biological system that are not clearly distinguishable by conventional methods. Furthermore, NC-PCA can identify these distinct characteristics without the express need for extra smoothing and does not distort the underlying data.

While the minimum resolution between two gaussian signals is the average of the linewidths of the signals, the detector resolution and pixel density per lifetime is also a key consideration. In order to determine the lifetime, the lifetime distribution must be fit to a gaussian of the form $f(x) = A \exp(-(x-\mu)^2/2s^2)$ where μ is the mean, s is the standard deviation or linewidth, and A is a normalization factor. In other words, if a more accurate lifetime is desired, the linewidth of the distribution must become narrower, and therefore the total number of pixels in the image attributed to that lifetime must increase in order to maintain a minimum number of data points and have a high quality fit. Based on the interdependence of these three factors, as pixel density or SNR of the signal increase (by improving detector performance or increasing the photon counts), the lifetime distribution linewidth decreases, improving the resolution.

To explore the possible dependence of NC-PCA on detector and imaging system, FLIM data was acquired from two different imaging systems (Zeiss and Olympus). In addition to studying the impact of the two instruments in the reconstruction process, several different biological and chemical conditions were investigated, including using a range of therapeutics, therapeutic concentrations, and media composition (see Table S4). All data are presented in Figures S11-S15.

Using these results, we calculated the median G and fB values and the STD mean values on a per image level, and the results are presented in Figure S16. In addition, to directly connect NC-PCA findings to imaging resolution and to evaluate the data set on a more holistic level, we calculated the linewidth values for the highest concentrations of all the treatments. This same calculation is performed for the STD mean values and G median values. The results are presented in Fig. 8 and Figure S17. Across all experimental conditions and both imaging systems, the NC-PCA reduces the STD mean value and the linewidth without modifying the median G value (Fig. 8, Figure S16- S17). This finding mirrors results shown in Fig. 6, demonstrating that NC-PCA effectively removes noise without loss of information and that NC-PCA can be universally applied, independent of imaging system or experimental conditions.

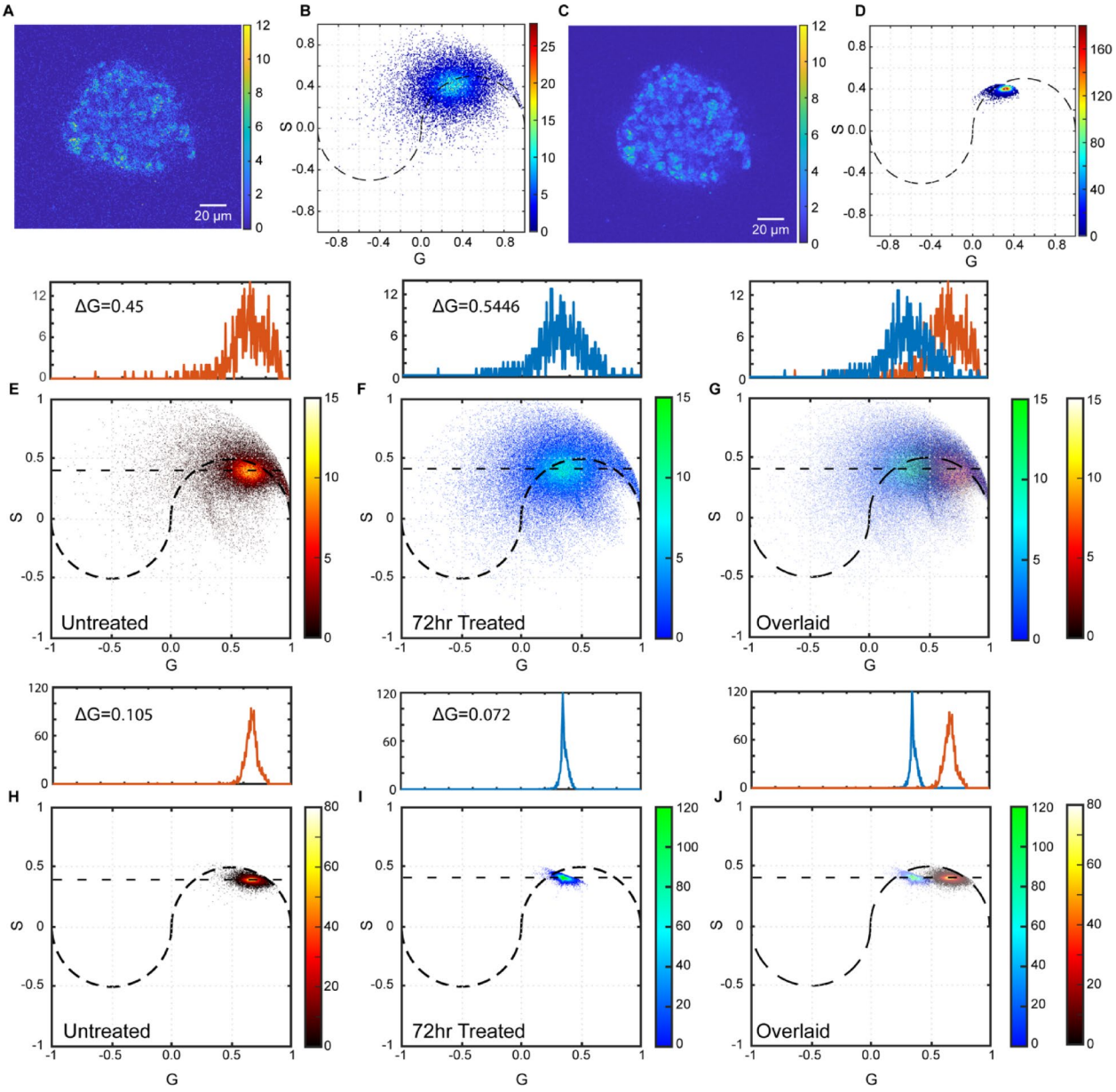

Fig. 7. Detecting time dependent effects of STS on patient-derived colorectal cancer organoid metabolism. First time bin and corresponding phasor histogram of an untreated patient-derived colorectal cancer organoid data analyzed using (**A**, **B**) TPA approach or (**C**, **D**) NC-PCA approach. Data was taken using 10-frame acquisition. (**E**) Phasor histograms of untreated and (**F**) 72-hour, 10μM STS-treated organoids analyzed using the FPA approach. (**G**) The phasor histograms in parts (**E**) and (**F**) are overlaid. The count distributions along the maximum count lines are fit to Gaussian distributions. (**H**, **I**) The same data set is analyzed using the NC-PCA approach, and (**J**) the pair of phasor histograms are overlaid. The count distributions along the maximum count lines are fit to Gaussian distributions.

Discussion

Fluorescence Lifetime Imaging Microscopy (FLIM) is an important tool for studying complex biological phenomena, but its effectiveness is often hindered by noise, acquisition time, and photodamage. One of the primary challenges of FLIM analysis is achieving high signal fidelity while minimizing these limiting factors. An effective analytical tool should not only preserve data fidelity, but also adaptively suppress noise, particularly when photon counts are low.

Here, we demonstrate that NC-PCA effectively mitigates noise distortion while preserving the underlying signal in time-series FLIM data. A key advantage of this method is its adaptivity through data-driven decomposition and its compatibility with standard FLIM data analysis workflows, allowing it to handle large FLIM datasets efficiently without extensive manual intervention or modification of current experimental protocols. This streamlining makes NC-PCA ideal for high-throughput FLIM studies. Furthermore, by

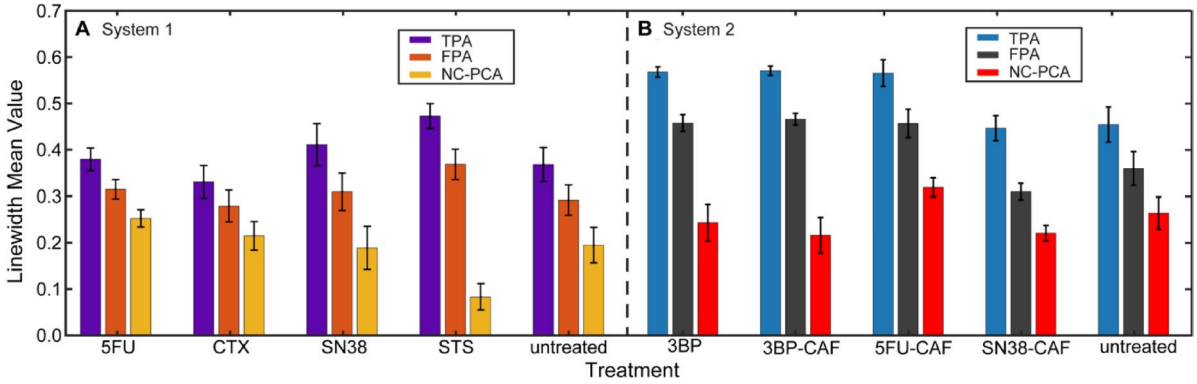

Fig. 8. Comparison of linewidth values of G coordinates across all the therapeutics and experimental conditions for the highest concentrations processed using TPA, FPA and NC-PCA methods for two different imaging systems. **(A)** Calculated linewidth values for all the therapeutics. Data taken using System 1 (Zeiss 780). **(B)** Calculated linewidth values for all the therapeutics. Data taken using System 2 (Olympus FV3000). As clearly observed, NC-PCA reduces the linewidth, improving the resolution of imaging. This enhancement is independent of the imaging system or experimental conditions.

reducing reliance on predefined settings, NC-PCA adjusts to varying data characteristics, ensuring consistent performance and enhancing reproducibility across different datasets. This makes NC-PCA a powerful tool for large-scale FLIM studies.

Another important advantage of NC-PCA is its compatibility with widely used filtering methods such as median, exponential, and average filtering. NC-PCA can be seamlessly combined with these filters in a hybrid mode to achieve a stronger improvement in the signal-to-noise ratio (SNR) of the biologically relevant signals. However, the main drawback of such combined approaches is the risk of over-smoothing, which can erase genuine variations and subtle features within the data. Therefore, careful optimization is essential to maximize noise suppression while preserving the integrity of meaningful information.

In addition, NC-PCA significantly broadens the scope of analytical operations that were previously limited to high photon count datasets. Using patient-derived colorectal cancer organoids, we demonstrated an average 10 dB improvement in SNR and a 10-fold reduction in MSE, highlighting NC-PCA's effectiveness in improving data fidelity.

These findings demonstrate that NC-PCA improves the accuracy by lowering per-pixel variance in phasor coordinates and improves the precision by increasing the pixel retention or the effective number of relevant denoised pixels used to calculate the phasor. As a result, NC-PCA improves the precision of the phasor-cloud centroid while keeping central value unchanged. Thus, NC-PCA facilitates the efficient and accurate application of advanced techniques such as reference-free calibration, multi-exponential lifetime fitting, fluorescence lifetime-resolved anisotropy, Förster Resonance Energy Transfer (FRET) analysis, and machine-learning-based FLIM analysis[35,36,39,40].

One major challenge in fluorescence imaging is balancing SNR against photodamage risk. Intense or prolonged laser exposure can generate reactive oxygen species, disrupt cellular function, and degrade fluorophores, limiting imaging duration and reliability[41,42]. NC-PCA mitigates these issues by increasing the SNR up to 20 dB in datasets even under low photon-count conditions, enabling reduced laser power and shorter acquisition times without compromising data quality. This preserves fluorophore integrity, minimizes photodamage, and enables repeated or long-term measurements essential for tracking dynamic processes like stem cell differentiation, drug response, or tumor progression[40,43,44].

Taken together, these findings establish NC-PCA as a powerful and enabling tool for both fundamental biological research and translational applications. Its ability to extract high-fidelity lifetime data from low photon-count FLIM images enhances precision in detecting metabolic states, disease progression, and therapeutic response, broadening its impact in biomedical research[36,40,43–47].

Methods

Data analysis methods

The FLIM data was analyzed using TPA, FPA, and NC-PCA through custom Python and MATLAB scripts. Notably, both scripts operate independently and produce identical results. Both the Python and MATLAB scripts are freely available on Zenodo (https://doi.org/10.5281/zenodo.14895223). While both scripts primarily process raw time-series TIFF files, they are designed for customization and adaptability. The algorithm implementation in both Python and MATLAB consists of three main components: a data preprocessing script, an NC-PCA analysis script, and a phasor analysis script. Adapting non-TIFF file formats for compatibility with the NC-PCA and phasor analysis scripts simply requires converting the imported data into arrays.

The TPA workflow is the simplest of the three. This method takes time-series FLIM data and applies an intensity (integrated counts) threshold and processes the data through phasor analysis. Intensity thresholding is performed by summing the total counts per pixel over time, applying a minimum count threshold, and setting all pixel values at or below that threshold to zero across each time bin.

The FPA workflow incorporates both intensity thresholding (as defined above) and median filtering. The median filter is applied to the phasor histogram, a common practice in similar applications. A kernel or window size is specified, determining the number of local data points used for filtering. While intensity thresholding is performed before any phasor transformation, the median filter is applied in phasor space and is included as a functionality in both the Python and MATLAB phasor analysis scripts.

The NC-PCA workflow begins by defining the number of principal components for projecting the raw data. For this study, we found that three principal components optimally preserved signal while removing noise. The script then applies the noise-correction (NC) scheme and stores the NC factors for later use. Both the Python and MATLAB scripts also allow tunability in the PCA method selection, depending on dataset size and computational efficiency. For this research, we used Singular Value Decomposition to extract the principal components. Once the dataset was flattened and the principal components were extracted, the original data was projected onto the new basis. The NC factors are then factored into the transformed dataset to properly scale the data back into its original state. Finally, the same intensity thresholding used in TPA and FPA was applied to ensure consistency across all methods. More information on the data analysis methods can be found in the SI.

Creation of synthetic FLIM data

A series of synthetic images were first created in PowerPoint. Three distinct images were designed to contain: (1) mitochondria and ribosomes, (2) the nucleus and vacuoles, and (3) the cell wall. When combined, these images mimicked a basic cell structure with distinct geometric features. By initially keeping them separate, we could independently tune the lifetime characteristics associated with each component set. Each image was assigned a lifetime and projected into 256-time bins with signals decaying exponentially according to their specified lifetimes. Once the temporal behavior was modeled, the three time-series datasets were merged into a single dataset.

To ensure that noise in the synthetic data accurately matched experimental data, we applied a Poisson noise distribution. Commonly known as Shot noise, the dominant noise source in FLIM data arises from photon counting errors with a standard deviation proportional to the square root of photon counts. Importantly, time-correlated single-photon detectors count photons independently of time bins. As a result, shot noise is temporally uncorrelated with dependencies only arising from the signal's exponential decay. To simulate this noise profile, we applied a randomized Poisson distribution to each pixel[30], setting the mean value to match the corresponding time-bin photon count. Additionally, to prevent zero standard deviation and ensure nonzero noise levels, a mean value of 0.8 (λ =0.8 for Poisson distribution) was assigned to background pixels with no fluorescent lifetime. This value was selected based on experimental results (see SI).

Since the signal-to-noise ratio (SNR) of shot noise scales with the square root of photon counts, we varied noise characteristics by adjusting the total photon count per pixel. The total counts per image were chosen to reflect experimental datasets, ranging from 80 to 1,800 photons. This approach ensured that our calculated noise accurately modeled variations encountered in experimental FLIM data while also testing the upper and lower limits of NC-PCA. Additional details on synthetic FLIM dataset construction are provided in the SI.

Sample preparation protocols

Coumarin-6 dye

Coumarin-6 (Sigma Aldrich #442631) reconstituted in 200 proof ethanol was used as the calibration standard before each imaging session.

Organoid culture

Patient-derived tumor organoids (PDTOs) were generated from colorectal cancer (CRC) tumor resections received from the USC Norris Comprehensive Cancer Center Translational Pathology Core according to Institutional Review Board (Protocol HS-06-00678) approval. Tissues were processed as outlined previously[43,44]. PDTOs were grown at 37 °C and 5% CO_2 in media which contained supplements as outlined in reference[36]. Additional details are in Table S3.

Sample preparation for FLIM imaging was also done according to previous publications. Briefly, organoids were dissociated into single cells by dissolving BME with Gentle Cell Dissociation Reagent (STEMCELL Technology, Cambridge, MA; 07174) at 4 °C with rocking for 30–40 min. A P-1000 pipette tip was used to break up the organoid fragments before centrifuging at 300xg for 5 min and replacing supernatant with 1:1 PBS: TrypLE (Thermofisher Scientific, Waltham, MA; 12605028 spiked with Y-27632 (STEMCELL Technology, Cambridge, MA; 72302) at 1:1000 dilution. The cell suspension was passed through a 40 µm cell strainer before isolating the cell pellet through centrifugation and resuspending in CTO media. 1000 cells/well were plated in a glass-bottom 96 well plate (Mattek, Ashland, MA; P96G-1.5-5-F) and grown in CTO media for 7 days before treatment.

Cells were dosed with various concentrations of Staurosporine (STS; Sigma-Aldrich, St. Louis, MO; 569396), 5-fluorouracil (5-FU; Selleck Chemicals, S1209), 7-ethyl-10-hydroxycamtothecin (SN-38; Sigma-Aldrich, St. Louis, MO; H0165), 3-bromopyruvate (3-BP; Sigma-Aldrich, St. Louis, MO; 16490), or cetuximab (CTX, MedChemExpress, Monmouth Junction, NJ; HY-P9905). Untreated controls for STS, SN-38 and 5-FU were wells of 0.01% DMSO in CTO media. Details on the dosing schedule and quantities are in Table S3. Treatments were applied 72 h before the first imaging sessions, and imaging was performed. All therapeutic concentrations were created using serial dilution.

FLIM imaging protocols

For all the data presented in the main text, except a portion of the data in Fig. 8, S15, and S17, an Olympus FV3000 system equipped with an A320 FastFLIM FLIMbox (ISS Inc., Champaign, IL) with a 10 µs/pixel

dwell time, hybrid PMT external detectors (Hamamatsu, Shizuoka, Japan), and a Ti: Sapphire 2-photon laser (Spectra-Physics, Mountain View, CA) was used with excitation at 740 nm. For this system, an Olympus UPLXAP020 × (20X NA 0.8) objective was used to capture FLIM images with 256 × 256 pixels. A 458/64 nm dichroic was used to collect the emission of NAD(P)H.

The second imaging system used to acquire a portion of the data in Fig. 8, S15, and S17 was located in a separate imaging facility. This was a Zeiss 780 inverted confocal microscope (Carl Zeiss, Jena, Germany) also with a A320 FastFLIM FLIMbox. The images were 256 × 256 pixels and were taken with a Plan-Apochromat M27 20X/0.8 NA (Carl Zeiss, Jena, Germany) objective at 12.6 µs/pixel dwell time. The PDTO samples were excited with a Ti: Sapphire 2-photon laser (Coherent Chameleon Ultra II) set at 740 nm for NAD(P)H excitation. The emission was split into two channels with a 590 nm long-pass filter, and each channel was further filtered at 460/80 nm for NAD(P)H. External photomultiplier tube detectors (Hamamatsu, Japan R10467U-40) were used to detect the emission for each channel.

In both systems, VistaVision software (ISS Inc., Champaign, IL) was used to collect the data. Table S5 lists all systems and settings and the corresponding data sets with additional meta-data. For every patient derived organoid presented in the main text, three z-slices with a step-size of 10 µm from the center (20 µm total imaged z-area) were imaged on both systems with a laser power of 15–20 mW. Samples were kept at 37 °C with 5% CO_2 for the entirety of the experiment.

For Coumarin-6 measurements, we used a 100-frame FLIM image taken as high signal to noise ratio reference data acting as the ground truth. To acquire the low signal to noise ratio Coumarin-6 image, we used 30-frame averaging. Next for both the reference data and raw data we performed a thresholding step to remove pixels with low counts which was followed by a per pixel single exponential fitting. Next the low-frame data (30-frame) was processed using NC-PCA method, and a per pixel exponential fitting was performed on the denoised pixels. The PDTO FLIM dataset in Figs. 5, 6 and 7 were originally published in our previous work and is used here for secondary analysis[36].

The images used as reference data were taken at 100-frame averaging, and the raw images used for denoising were taken at 10-frame averaging.

Data availability

All the data, codes and materials needed for this study are available on Zenodo (https://doi.org/10.5281/zenodo.14895223).

Received: 16 July 2025; Accepted: 10 October 2025
Published online: 17 November 2025

References

1. Shirshin, E. A. et al. Label-free sensing of cells with fluorescence lifetime imaging: The quest for metabolic heterogeneity. *Proceedings of the National Academy of Sciences* 119, e2118241119 (2022).
2. Bowman, A. J., Huang, C., Schnitzer, M. J. & Kasevich, M. A. Wide-field fluorescence lifetime imaging of neuron spiking and subthreshold activity in vivo. *Science* **380**, 1270–1275 (2023).
3. Okkelman, I. A., Papkovsky, D. B. & Dmitriev, R. I. Estimation of the mitochondrial membrane potential using fluorescence lifetime imaging microscopy. *Cytometry Part. A*. **97**, 471–482 (2020).
4. Harpur, A. G., Wouters, F. S. & Bastiaens, P. I. H. Imaging FRET between spectrally similar GFP molecules in single cells. *Nat. Biotechnol.* **19**, 167–169 (2001).
5. Murakoshi, H., Lee, S. J. & Yasuda, R. Highly sensitive and quantitative FRET–FLIM imaging in single dendritic spines using improved non-radiative YFP. *Brain Cell. Bio*. **36**, 31–42 (2008).
6. Huang, M. et al. Carbon dots for Intracellular pH sensing with fluorescence lifetime imaging microscopy. *Nanomaterials* 10, (2020).
7. Deng, D. et al. Quantitative profiling pH Heterogeneity of acidic endolysosomal compartments using fluorescence lifetime imaging microscopy. *MBoC* mbc.E23-06-0220 (2025). https://doi.org/10.1091/mbc.E23-06-0220
8. Okabe, K. et al. Intracellular temperature mapping with a fluorescent polymeric thermometer and fluorescence lifetime imaging microscopy. *Nat. Commun.* **3**, 705 (2012).
9. Ziomkiewicz, I. et al. Dynamic conformational transitions of the EGF receptor in living mammalian cells determined by FRET and fluorescence lifetime imaging microscopy. *Cytometry Part. A*. **83**, 794–805 (2013).
10. Ma, Y. et al. Light-field tomographic fluorescence lifetime imaging microscopy. *Proceedings of the National Academy of Sciences* 121, e2402556121 (2024).
11. Theodossiou, A., Alex, J. & Jocelyn Martinez, & Walsh. Fast autofluorescence imaging to evaluate dynamic changes in cell metabolism. *J. Biomed. Opt.* **29**, 126501 (2024).
12. Blacker, T. S. et al. Separating NADH and NADPH fluorescence in live cells and tissues using FLIM. *Nat. Commun.* **5**, 3936 (2014).
13. Stringari, C. et al. Phasor approach to fluorescence lifetime microscopy distinguishes different metabolic States of germ cells in a live tissue. *Proc. Natl. Acad. Sci.* **108**, 13582–13587 (2011).
14. BECKER, W. Fluorescence lifetime imaging—techniques and applications. *J. Microsc.* **247**, 119–136 (2012).
15. Datta, R., Heaster, T. M., Sharick, J. T., Gillette, A. A. & Skala, M. C. Fluorescence lifetime imaging microscopy: Fundamentals and advances in instrumentation, analysis, and applications. *J. Biomed. Opt.* **25**, 1 (2020).
16. Ranjit, S., Datta, R., Dvornikov, A. & Gratton, E. Multicomponent analysis of phasor plot in a single pixel to calculate changes of metabolic trajectory in biological systems. *J. Phys. Chem. A*. **123**, 9865–9873 (2019).
17. Digman, M. A., Caiolfa, V. R., Zamai, M. & Gratton, E. The phasor approach to fluorescence lifetime imaging analysis. *Biophys. J.* **94**, L14–L16 (2008).
18. Rahim, M. K. et al. Phasor analysis of fluorescence lifetime enables quantitative multiplexed molecular imaging of three probes. *Anal. Chem.* **94**, 14185–14194 (2022).
19. Mannam, V., Brandt, P., Smith, J., Yuan, C. J. & Howard, S. X. Improving fluorescence lifetime imaging microscopy phasor accuracy using convolutional neural networks. *Front. Bioinformat.* **3**, (2023).
20. Wang, P. et al. Complex wavelet filter improves FLIM phasors for photon starved imaging experiments. *Biomed. Opt. Express.* **12**, 3463–3473 (2021).
21. Warren, S. C. et al. Rapid global fitting of large fluorescence lifetime imaging microscopy datasets. *PLOS ONE.* **8**, e70687 (2013).

22. Donoho, D. L., Johnstone, I. M. & and Adapting to unknown smoothness via wavelet shrinkage. *J. Am. Stat. Assoc.* **90**, 1200–1224 (1995).
23. Zhang, K., Zuo, W., Chen, Y. & Meng, D. Zhang. Beyond a Gaussian denoiser: Residual learning of deep CNN for image denoising. *IEEE Trans. Image Process.* **26**, 3142–3155 (2017).
24. Liu, H. et al. A fusion of principal component analysis and singular value decomposition based multivariate denoising algorithm for free induction decay transversal data. *Rev. Sci. Instrum.* **90**, 035116 (2019).
25. Abdoli, A., Stoyanova, R. & Maudsley, A. A. Denoising of MR spectroscopic imaging data using statistical selection of principal components. *Magn. Reson. Mater. Phys., Biol. Med.* **29**, 811–822 (2016).
26. David, C. C. & Jacobs, D. J. Principal component analysis: A method for determining the essential dynamics of proteins. in Protein Dynamics: Methods and Protocols (ed Livesay, D. R.) 193–226 (Humana, Totowa, NJ, doi:https://doi.org/10.1007/978-1-62703-658-0_11. (2014).
27. Le Marois, A., Labouesse, S., Suhling, K. & Heintzmann, R. Noise-Corrected principal component analysis of fluorescence lifetime imaging data. *J. Biophotonics*. **10**, 1124–1133 (2017).
28. de Miranda, A. M. F. L., de Seixas, J. M., Junior, C., Ferreira, J. D., Cerqueira, A. S. & D. D. & A principal component-based algorithm for denoising in single channel data (PCA for denoising in single channel data). *Measurement* **60**, 121–128 (2015).
29. Guo, Q., Zhang, C. & Zhang, Y. Liu. An efficient SVD-based method for image denoising. *IEEE Trans. Circuits Syst. Video Technol.* **26**, 868–880 (2016).
30. Walsh, A. J., Sharick, J. T., Skala, M. C. & Beier, H. T. Temporal Binning of time-correlated single photon counting data improves exponential decay fits and imaging speed. *Biomed. Opt. Express*. **7**, 1385 (2016).
31. Gerritsen, H. C., Agronskaia, A. V., Bader, A. N. & Esposito, A. Chapter 3 Time domain FLIM: Theory, instrumentation, and data analysis. in *Laboratory Techniques in Biochemistry and Molecular Biology* vol. 33 95–132 (Elsevier, 2009).
32. O'Connor, D. V. & Phillips, D. 2 Basic principles of the single photon counting lifetime measurement. in Time-Correlated Single Photon Counting (eds O'Connor, D. V. & Phillips, D.) 36–54 (Academic, doi:https://doi.org/10.1016/B978-0-12-524140-3.50006-X. (1984).
33. Kristoffersen, A. S., Erga, S. R., Hamre, B. & Frette, Ø. Testing fluorescence lifetime standards using two-photon excitation and time-domain instrumentation: Rhodamine B, coumarin 6 and Lucifer yellow. *J. Fluoresc.* **24**, 1015–1024 (2014).
34. Raikar, U. S. et al. Solvent effects on the absorption and fluorescence spectra of coumarins 6 and 7 molecules: Determination of ground and excited state dipole moment. *Spectrochim. Acta Part A Mol. Biomol. Spectrosc.* **65**, 673–677 (2006).
35. Song, A. et al. Visualizing subcellular changes in the NAD(H) pool size versus redox state using fluorescence lifetime imaging microscopy of NADH. *Commun. Biol.*. **7**, 428 (2024).
36. Tavakoli, N. et al. Merging metabolic modeling and imaging for screening therapeutic targets in colorectal cancer. *Npj Syst. Biol. Appl.* **11**, 12 (2025).
37. Malacrida, L., Ranjit, S., Jameson, D. M. & Gratton, E. The phasor plot: A universal circle to advance fluorescence lifetime analysis and interpretation. *Annual Rev. Biophys.* **50**, 575–593 (2021).
38. Lakowicz, J. R., Szmacinski, H., Nowaczyk, K. & Johnson, M. L. Fluorescence lifetime imaging of free and protein-bound NADH. *Proc. Natl. Acad. Sci. USA*. **89**, 1271–1275 (1992).
39. Frei, M. S., Koch, B., Hiblot, J. & Johnsson, K. Live-Cell fluorescence lifetime multiplexing using synthetic fluorescent probes. *ACS Chem. Biol.* **17**, 1321–1327 (2022).
40. Pal, R. et al. Fluorescence lifetime of injected indocyanine green as a universal marker of solid tumours in patients. *Nat. Biomedical Eng.* **7**, 1649–1666 (2023).
41. Yokoi, Y. et al. Potential consequences of phototoxicity on cell function during live imaging of intestinal organoids. *Plos One*. **19**, e0313213 (2024).
42. Icha, J., Weber, M., Waters, J. C. & Norden, C. Phototoxicity in live fluorescence microscopy, and how to avoid it. *BioEssays* **39**, 1700003 (2017).
43. Kim, S. et al. Comparison of cell and organoid-level analysis of patient-derived 3D organoids to evaluate tumor cell growth dynamics and drug response. *SLAS Discovery*. **25**, 744–754 (2020).
44. Garvey, C. M. et al. Anti-EGFR Therapy Induces EGF Secretion by Cancer-Associated Fibroblasts to Confer Colorectal Cancer Chemoresistance. *Cancers* 12, (2020).
45. Ma, N., Digman, M. A., Malacrida, L. & Gratton, E. Measurements of absolute concentrations of NADH in cells using the phasor FLIM method. *Biomed. Opt. Express*. **7**, 2441–2452 (2016).
46. Rodimova, S. et al. Mapping metabolism of liver tissue using two-photon FLIM. *Biomed. Opt. Express*. **11**, 4458 (2020).
47. Nobis, M. et al. Intravital FLIM-FRET imaging reveals Dasatinib-Induced Spatial control of Src in pancreatic cancer. *Cancer Res.* **73**, 4674–4686 (2013).

Acknowledgements

We would like to thank the members of the Ellison Medical Institute for scientific discussions, and a special thanks to the Cell Line Team (Michael Doche, Roy Lau, Scott Valena and Pratiksha Kshetri) for cell culture assistance. We would like to thank Dr. Heinz-Josef Lenz and his lab members at the USC Keck School of Medicine for providing access to colorectal cancer patient tissues. We would also like to acknowledge the USC Norris Comprehensive Cancer Center Translational Pathology Core and the Molecular Genomics Core for the collection of patient tissue samples and targeted sequencing of our patient organoid lines (Norris Comprehensive Cancer Center CCSG grant, P30CA014089).

Author contributions

S.S conceived and designed the study, acquired Coumarin-6 and spheroid low count and ground truth data, performed data analysis, resolution and noise studies and Coumarin-6 lifetime fitting in MATLAB. J.G.P performed analysis, noise studies and created and analyzed the synthetic data in Python. E.J.F took the box plot data. A.M.A and S.M.M supervised the project. S.S, J.G.P and A.M.A wrote the manuscript with contributions from all the authors.

Funding

We acknowledge financial support from: Office of Naval Research (N00014-24-1-2296), National Science Foundation (DBI-2414158), and National Cancer Institute Cancer Systems Biology Consortium (U01CA232137).

Declarations

Competing interests

Shannon M. Mumenthaler is the Chief Translational Research Officer for the Ellison Medical Institute. Andrea M. Armani is the Senior Director, Physical Sciences and Engineering at the Ellison Medical Institute. Emma Fong is a Research Scientist at the Ellison Medical Institute. Soheil Soltani is a Research Scientist at the Ellison Medical Institute. The other authors declare no competing interests.

Consent to participate

The use of patient samples was reviewed and approved by the University of Southern California Biomedical Institutional Review Board, under protocol number HS-06–00678. All patients provided written informed consent prior to sample collection. Samples were de-identified to research staff.

Ethics approval

Experimental protocol approval: All the experimental protocols were carried out in accordance with Institutional Review Board (Protocol HS-06-00678) approval. Method approval: All methods were carried out in accordance with the guidelines and regulations set in the Ellison Medical Institute Umbrella Biohazardous Use Authorization approved by the Institutional Biosafety Committee.

Additional information

Supplementary Information The online version contains supplementary material available at https://doi.org/10.1038/s41598-025-24022-7.

Correspondence and requests for materials should be addressed to A.M.A.

Reprints and permissions information is available at www.nature.com/reprints.

Publisher's note Springer Nature remains neutral with regard to jurisdictional claims in published maps and institutional affiliations.